Available online at www.sciencedirect.com

SciVerse ScienceDirect

Geochimica et Cosmochimica Acta 85 (2012) 357–372

Geochimica et Cosmochimica Acta

www.elsevier.com/locate/gca

Effect of H_2O on the density of silicate melts at high pressures: Static experiments and the application of a modified hard-sphere model of equation of state

Zhicheng Jing [a,b,*], Shun-ichiro Karato [b]

[a] Center for Advanced Radiation Sources, The University of Chicago, Argonne, IL 60439, USA
[b] Department of Geology and Geophysics, Yale University, New Haven, CT 06520, USA

Received 16 March 2011; accepted in revised form 1 March 2012; available online 13 March 2012

Abstract

Density of ultramafic silicate melts was determined using the sink/float technique at high pressures. Seven melt compositions were studied, among which three were dry compositions with different Mg#'s (molar MgO/(MgO + FeO) × 100) and the other four were hydrous compositions synthesized by adding 2–7 wt.% H_2O to the anhydrous ones. Experimental conditions range from 9 to 15 GPa and from 2173 to 2473 K. The sinking and floatation of density markers were observed for all melt compositions. Melt density data were analyzed by applying the Birch–Murnaghan equation of state and a newly developed equation of state for silicate melts based on the model of hard sphere mixtures. The presence of water can significantly reduce the density of melts due to its small molecular mass. On the other hand, water makes hydrous silicate melts more compressible than anhydrous melts and therefore the effect of H_2O on melt density is less significant at high pressures. The density of hydrous melts was then calculated as a function of H_2O content at the conditions of the bottom of the upper mantle, and was compared with the density of the dominant upper mantle minerals. Results show that the conditions for a negatively buoyant melt that coexists with a pyrolite mantle atop the 410 km discontinuity are marginally satisfied if H_2O is the only volatile component to facilitate melting, but such conditions will be satisfied by a broader range of conditions when other heavier volatile elements (C, K, etc.) are also present.

1. INTRODUCTION

The density contrast between melts and surrounding solids determines the direction of material transport in the Earth and therefore the density of silicate melts plays a very important role in controlling the chemical differentiation of the Earth. Stolper et al. (1981) suggested that the density of silicate melts may exceed that of the coexisting solids in the deep upper mantle due to the much higher compressibility of liquids than that of solids. This hypothesis has been confirmed by various measurements on the density of anhydrous melts for a range of compositions using both static compression (e.g., Agee and Walker, 1988, 1993; Suzuki et al., 1995; Agee, 1998; Ohtani et al., 1998; Suzuki et al., 1998; Ohtani and Maeda, 2001) and shock-wave techniques (e.g., Rigden et al., 1988, 1989; Miller et al., 1991). The presence of gravitationally stable deep melts near 410 km depth and at the base of the lower mantle has also been suggested based on some seismological observations (e.g., Revenaugh and Sipkin, 1994; Williams and Garnero, 1996).

However, it is difficult to generate silicate melts in the deep mantle since the solidus temperature increases significantly as pressure increases (Takahashi, 1986; Zhang and Herzberg, 1994). Therefore melting in the deep mantle likely involves the participation of volatile components especially water which reduces the solidus of the mantle

* Corresponding author at: Center for Advanced Radiation Sources, The University of Chicago, Argonne, IL 60439, USA. Tel.: +1 630 252 0435; fax: +1 630 252 0436.
E-mail addresses: zjing@uchicago.edu, jing@cars.uchicago.edu (Z. Jing).

0016-7037/$ - see front matter © 2012 Elsevier Ltd. All rights reserved.
http://dx.doi.org/10.1016/j.gca.2012.03.001

(Kawamoto and Holloway, 1997; Litasov and Ohtani, 2002). However, this implies that the melt produced in the deep mantle conditions should contain volatile elements and therefore the influence of volatile elements on density needs to be considered when one evaluates whether the density crossover occurs or not. It is therefore critical to investigate the influence of water on melt density at high pressures.

To date, only a limited number of density measurements are available for a few hydrous melt compositions due to the difficulty in confining water at high temperature and pressure conditions. Burnham and Davis (1971) directly determined the density of hydrous albite melts up to 0.84 GPa using an internally heated pressure vessel. By measuring the density of quenched glasses as a function of temperature, Ochs and Lange (1997, 1999) obtained the density of hydrous albite, rhyolite and KCS (K_2O–CaO–SiO_2) liquids at their glass transition temperatures. These studies at low pressures show that water can significantly reduce the density of melts due to the small partial molar density of the H_2O component. On the other hand, water can also make the melts more compressible as suggested by the results of Ochs and Lange (1997, 1999). Recent measurements on the density of hydrous ultramafic, peridotitic, and basaltic melts at mantle pressures using the sink/float technique (Matsukage et al., 2005; Sakamaki et al., 2006; Agee, 2008) and the X-ray absorption technique (Sakamaki et al., 2009) confirmed that the influence of water is less significant (although still important) compared to that at low pressure conditions.

Using these density data at various pressures, the equation of state (EOS) for hydrous silicate melts may be obtained. One such attempt employs the third-order Birch–Murnaghan EOS (Jing and Karato, 2008, 2009) in conjunction to the ideal-mixing model for molar volume and compressibility to discuss the effect of water on density under the conditions of Earth's upper mantle. However, the EOS for H_2O-bearing silicate melts could not be fully constrained due to the scarcity of density data and the lack of bulk modulus (sound velocity) data. In addition, our recent study (Jing and Karato, 2011) shows that silicate liquids have very different compression mechanisms than those of solids and therefore a new EOS in accord with the compressional properties of silicate liquids is developed based on the modification of a hard sphere mixture model. It is the purpose of this study to expand the experimental data set on high-pressure melt density and to develop a new EOS for hydrous silicate melts.

2. EXPERIMENTAL METHODS

2.1. Starting materials

In order to determine the density of melts formed at 410 km depth, we explored a range of possible melt compositions. Matsukage et al. (2005) chose a melt composition with 35.5 wt.% SiO_2, 3.3 wt.% Al_2O_3, 11.6 wt.% FeO, 30.4 wt.% MgO, 14.1 wt.% CaO, and 5 wt.% H_2O as the target mantle melt composition based on the hydrous melting experiments by Litasov and Ohtani (2002) and Inoue and Sawamoto (1992). By adjusting the Mg# (molar $MgO/(MgO + FeO) \times 100$) of the melts, Matsukage et al. (2005) studied four hydrous melt compositions with 5 wt.% water. To further investigate the effect of water, we expand the composition range by adding water to or subtracting water from these compositions. Three dry compositions with Mg# of 77, 70, and 61, and four hydrous compositions with 2, 3, 5, and 7 wt.% H_2O are studied. The chemical compositions of the starting materials are listed in Table 1. The Mg# and H_2O content in the starting compositions are shown in Fig. 1 and compared with the compositions from Matsukage et al. (2005).

Starting materials were prepared from reagent grade oxide and hydroxide powders of SiO_2, Al_2O_3, FeO, MgO, $Mg(OH)_2$, and $Ca(OH)_2$. CO_2 contamination in the $Mg(OH)_2$ powder was confirmed to be negligible by measuring the weight loss after heating some $Mg(OH)_2$ powder at 1273 K overnight: more than 98% of weight loss could be attributed to dehydration instead of decarbonation. To prevent FeO from being oxidized to Fe_2O_3, FeO and MgO were mixed first and reacted in an oxygen-fugacity controlled furnace to make $(Mg_{0.25}Fe_{0.75})O$. For dry melt compositions, SiO_2 and $Ca(OH)_2$ were reacted to $CaSiO_3$ to add CaO to the system. For hydrous melt compositions, $Mg(OH)_2$, and $Ca(OH)_2$ were used to add water. Appropriate amounts of these reactants excluding the hydroxides were mixed in ethanol and ground in an agate mortar for about 2 h. The mixtures were then heated at 1473 K in a CO/CO_2 gas mixture at an oxygen fugacity between the WM (wüstite–magnetite) buffer and the IW (iron–wüstite) buffer, and about two orders of magnitude lower than the Ni–NiO buffer for 36 h. Hydroxides were then added to the mixtures and ground again for 2 h. The starting materials were then stored in a vacuum desiccator at ~413 K. This way of preparing starting materials can enhance the reaction kinetics and melting above the liquidus temperature.

2.2. Experimental setup and procedure

The sink/float technique (Agee and Walker, 1988) has been used to determine the density of silicate melts at high pressures. In this technique, the density of a melt is bracketed by the sinking and floatation of preloaded density markers in the melt. Single-crystal diamonds were used as density markers in this study. The density of diamonds was calculated using the third-order Birch–Murnaghan EOS.

$$P=\frac{3}{2}K_{T_0}\left[\left(\frac{\rho}{\rho_0}\right)^{7/3}-\left(\frac{\rho}{\rho_0}\right)^{5/3}\right]\left\{1+\frac{3}{4}(K'_{T_0}-4)\left[\left(\frac{\rho}{\rho_0}\right)^{2/3}-1\right]\right\}, \quad (1)$$

where ρ, ρ_0, K_{T_0}, and K'_{T_0} are the high-pressure density, room-pressure density, room-pressure bulk modulus, and the pressure derivative of bulk modulus at room pressure, respectively. High-temperature values of ρ_0, K_{T_0} were calculated from the coefficient of thermal expansion and the temperature derivative of K_{T_0}. All the parameters needed for the EOS of diamond were given in Suzuki et al. (1998).

The sink/float experiments were performed in a Kawai-type multianvil apparatus at Yale University. The truncation edge length (TEL) of the tungsten carbide anvils was

Table 1
Chemical compositions of the starting materials.

	Anhydrous compositions			Hydrous compositions			
	s3	s7	s6	s7_2	s6_3	s6_5	s6_7
SiO_2	36.8	36.1	35.2	35.4	34.2	33.5	32.7
Al_2O_3	3.4	3.3	3.3	3.3	3.2	3.1	3.0
FeO	16.0	20.9	26.8	20.5	26.0	25.5	24.9
MgO	30.0	27.1	23.7	26.5	23.0	22.5	22.1
CaO	13.8	12.6	11.0	12.3	10.7	10.5	10.2
H_2O	0.0	0.0	0.0	2.0	3.0	5.0	7.0
Total (wt.%)	100.0	100.0	100.0	100.0	100.0	100.0	100.0
Mg#	76.9	69.8	61.2	69.8	61.2	61.2	61.2

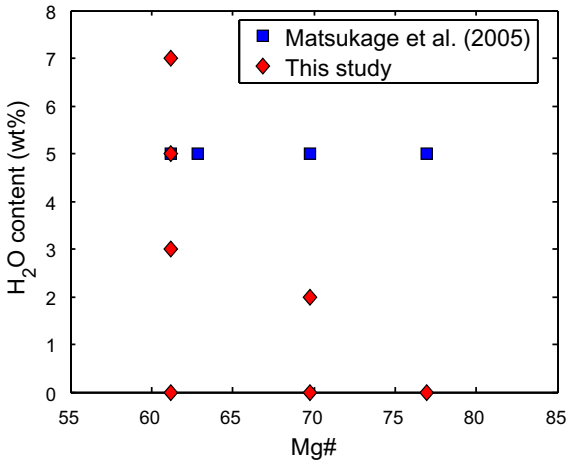

Fig. 1. Mg# and water content of the starting materials in this study (red diamonds) and in Matsukage et al. (2005) (blue squares). (For interpretation of the references to colour in this figure legend, the reader is referred to the web version of this article.)

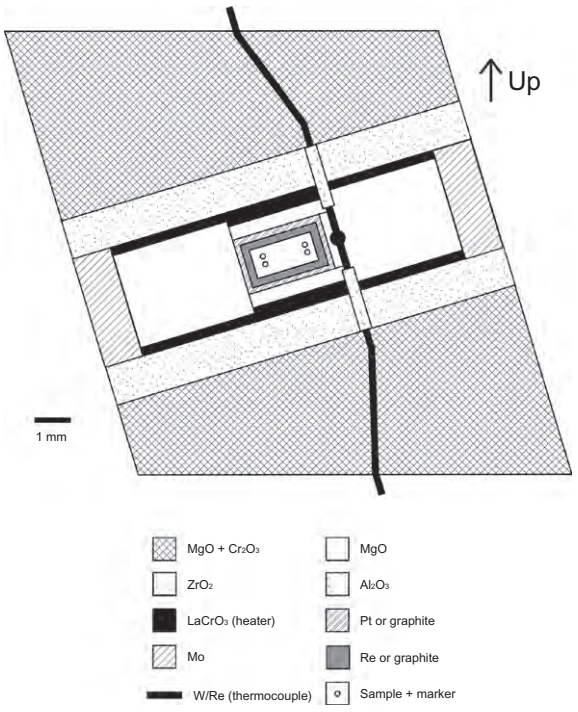

Fig. 2. Cross-section of the cell assembly for sink/float experiments. Re and Pt double capsules were used for experiments on hydrous melts while graphite capsules were used for dry experiments. Two diamonds were placed close to each end of the capsule.

8 mm, and the edge length of the octahedral pressure medium was 14 mm (14/8 assembly). The pressure-load relationship for this cell assembly was calibrated at 1573 K by the phase transition of SiO_2 from coesite to stishovite (Zhang et al., 1996) and the phase transition of Mg_2SiO_4 from olivine to wadsleyite (Morishima et al., 1994). The uncertainty in pressure is estimated to be about 0.5 GPa or ~5% due to the imperfect reproducibility in experiments.

Fig. 2 shows the cross-section of the cell assembly. For each experiment, four grains of single-crystal diamond with diameters about 120 μm were loaded with the starting materials into a sample capsule, with two grains placed close to each end of the capsule (see Fig. 2 for the positions of markers). Thus we can verify the movement of diamonds by observing the sinking or floatation of all four grains. Graphite sample containers with 1.0 mm I.D. (inner diameter) and 1.6 mm O.D. (outer diameter) were used for anhydrous melt compositions. For hydrous compositions, the sample material and density markers were first loaded into a Re inner capsule with 1.1 mm I.D. and 1.2 mm O.D. and mechanically shut. The Re capsule was then inserted into a Pt outer capsule with 1.2 mm I.D. and 1.4 mm O.D. and finally inserted into another Pt capsule with 1.4 mm I.D. and 1.6 mm O.D. which functions as a cover. The Pt capsules were then pressure sealed during compression. No welding was applied to avoid chemical reactions during the welding. This technique of confining water was demonstrated to be successful by Sumita and Inoue (1996) to pressure and temperature conditions up to 12 GPa and 2000 K. The sample capsule was then inserted into an MgO sleeve in the Cr_2O_3 doped MgO octahedral pressure medium. A stepped $LaCrO_3$ furnace was used to reduce the temperature gradient. The temperature was monitored by a $W_{95}Re_5$–$W_{74}Re_{26}$ thermocouple without correcting for the pressure effect on the thermocouple e.m.f. An MgO disc (~0.3 mm thick) was inserted between the thermocouple and the capsule to prevent the intrusion of the thermocouple and reaction between the thermocouple and the capsule materials. The cell assembly was positioned horizontally (Fig. 2) to further reduce the thermal gradient along the vertical direction,

which is more critical to the sink/float experiments. The horizontal temperature gradient along the cylindrical axis of the sample capsule is estimated to be less than 100 K. Considering that the thermal expansivity of melts is about 1×10^{-4} K^{-1} at room-pressure (Lange, 1997) and even smaller at high pressure (Suzuki et al., 1998), the density difference due to a 100 K temperature gradient will be less than 1%, which is smaller than the typical uncertainty in the sink/float experiments. In the worst-case scenario that the temperature gradient extends over the entire sample capsule and the melt density is very close to the density of diamond, then the diamonds near one end of the capsule may sink, and the ones near the other may float. This will then be considered as a neutral buoyancy case.

In each experiment, the sample was first compressed to a desired load at room temperature and was then heated at a rate of 50 K/min to 1273 K. After that, temperature was increased at a much higher rate, usually ~400–500 K/min, to the target temperature to minimize possible chemical reactions between the sample, the density markers and the capsule materials. Experimental durations were typically from ~30 to ~60 s for hydrous melts and from ~60 to ~300 s for anhydrous melts. The fast settling of the density markers is ensured by the low viscosity of the ultramafic melts, which is estimated to be about 0.01–0.05 Pa s at 2173 K and 9–15 GPa (Dingwell et al., 2004; Liebske et al., 2005) and likely lower for hydrous melts and at higher temperatures. Even if the density difference between the density markers and the liquid sample is as low as 1%, the 30-s duration is long enough for the density markers to move across the ~0.7 mm diameter capsule (capsule diameters are smaller at high pressures (Fig. 3)). Experiments were quenched isobarically by shutting off the heating power, with temperature dropped to lower than 800 K in less than 1 s. For each melt composition, a series of experiments were conducted at various pressures. Experimental conditions are from ~9 to ~15 GPa and from 2173 to 2473 K (Table 2).

It is important to demonstrate that water was preserved during the experiments at high-pressure and high-temperature conditions. However this is not a trivial task since the melts studied cannot be quenched to glasses due to the low viscosity at high temperature. We therefore conducted additional test experiments on a hydrous albite melt, which may be quenched to a hydrous glass and hence can be measured for its water content using Fourier transform infrared spectroscopy (FT-IR). The hydrous albite starting material was synthesized by mixing dry albite glass and distilled water using an 18/11 cell assembly at 5GPa and 1873 K for 10 min (Run K347). The run product of K347 (hydrous albite glass) was checked by FT-IR spectroscopy for water content and was cut into two pieces. The first piece was loaded into a Pt capsule similar to that used in the sink/float experiments for a test experiment at 5 GPa and 2073 K for 1 min (Run K965) to mimic the conditions of sink/float experiments for hydrous melts except that the pressure was lower. The second piece was used for a similar test experiment to Run K965 but at a higher pressure (15 GPa and 2173 K). Of these two test experiments, only the one at 5 GPa (K965) produced a glass that could be analyzed by FT-IR (see below). Jadeite crystals were found in the run product quenched from 15GPa.

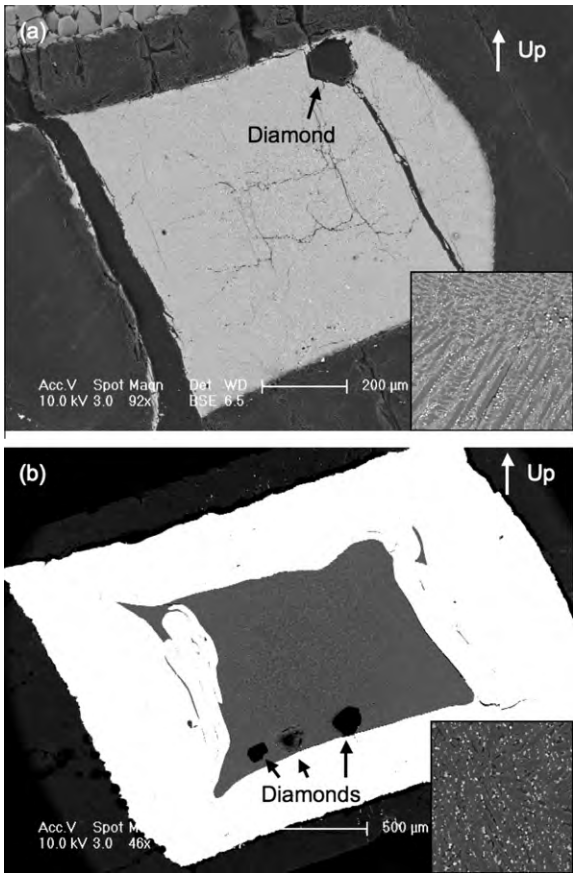

Fig. 3. Back-scattered electron images of run products. (a) Run K710 (Diamonds floated); (b) Run K680 (Diamonds sank). Insets are close-up views of the run products showing the quench crystals and interstitial glasses.

3. EXPERIMENTAL RESULTS

3.1. Sink/float brackets

After each experiment, the run product was sectioned parallel to the gravity direction and the axis of the cylindrical capsule. The sample was then polished and examined by both an optical microscope and a scanning electron microscope (SEM) in the back-scattered imaging (BEI) mode. Typical back-scattered electron images of run products for the anhydrous and hydrous melts are shown in Fig. 3a and b, respectively. The observations of quench crystals and interstitial glass in the run products (insets of Fig. 3a and b) confirm that samples were completely melted during the experiments. Bubbles or pores produced by the exsolution of water during cooling were also observed in the hydrous samples shown as the dark areas between the quench crystals in the BEI images (inset of Fig. 3b) indicating the presence of water during the experiments.

The density of melts can then be bracketed by the sinking and floatation of diamonds in the melts. There are cases

Table 2
Experimental conditions and results.

Composition	Run no.	Pressure (GPa)	Temperature (K)	Duration (s)	Marker density (g/cm^3)	Result
s3	K817	14.0	2473 ± 5	90	3.517	Sink
	K813	15.2	2473 ± 5	90	3.528	Float
s7	K710	11.8	2373 ± 10	60	3.504	Sink
	K721	14.0	2423 ± 10	60	3.523	Float
s6	K818	9.0	2473 ± 10	90	3.474	Sink
	K834	10.9	2473 ± 10	120	3.491	Neutral
	K847	11.8	2473 ± 15	300	3.498	Float
s7_2	K959	13.3	2173 ± 15	50	3.534	Sink
	K734	14.0	2173 ± 50	30	3.539	Neutral
	K739	15.2	2173 ± 20	40	3.549	Float
s6_3	K680	9.0	2168 ± 5	60	3.498	Sink
	K677	10.9	2167 ± 4	60	3.514	Float
	K671	12.6	2173 ± 10	60	3.527	Float
s6_5	K485	10.9	2173 ± 5	60	3.514	Sink
	K460	12.6	2173 ± 5	20	3.527	Float
s6_7	K958	11.8	2173 ± 10	40	3.521	Sink
	K756	12.6	2173 ± 10	60	3.527	Neutral
	K960	14.0	2163 ± 10	40	3.539	Neutral
	K727	14.6	2168 ± 5	40	3.544	Neutral
	K963	15.2	2163 ± 10	40	3.549	Float

when the positions of diamonds are between sinking and floating. These results are regarded as neutrally buoyant, that is, the density difference between the diamonds and the melt was too small for diamonds to settle. The results of all experiments are listed in Table 2. We consider the density of a melt as the density of diamond at the midpoint of the sinking and floatation pressures. If we define the upper and lower bounds as the melt compression curves passing through the sink and float brackets, then the uncertainties in density measurements are estimated to be the range in density between those two curves at the midpoint pressure. To estimate the uncertainties associated with this approach, we use a simple model of ideal mixing and the Birch–Murnaghan equation of state without justifying its applicability to hydrous silicate melts. As an example, the density of melt s7 (3.514 g/cm^3) at 12.9 GPa is constrained by the sinking of diamond (3.504 g/cm^3) at 11.8 GPa, and the floatation of diamond (3.523 g/cm^3) at 14.0 GPa. The room-pressure density and bulk modulus of melts can be estimated from the ideal mixing model as 2.771 g/cm^3 and 18.8 GPa (see next Section and Table 5 for the details of this calculation). If the Birch–Murnaghan EOS is applied to the melts, the upper and lower bounds for the melt density at 12.9 GPa are estimated to be 3.546 and 3.490 g/cm^3, respectively, which are offset by about 0.9% and 0.6% from the estimated density. Fig. 4 shows the compression curves for the density marker (diamond) and melt s7 at 2398 K and the calculated upper and lower bounds.

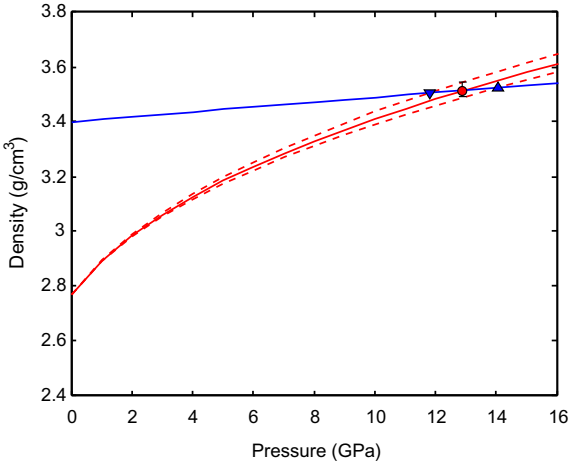

Fig. 4. Compression curves calculated using Birch–Murnaghan EOS for the diamond density marker (blue) and melt s7 (red) at 2398 K. Triangle pointing upwards indicates diamonds floated; Triangle pointing downwards indicates diamonds sank. Dashed lines represent the upper and lower bounds of the estimated density at various pressures based on the sinking and floatation of diamonds. (For interpretation of the references to colour in this figure legend, the reader is referred to the web version of this article.)

3.2. Run products

The composition of each run product was analyzed by an electron probe micro-analyzer (EPMA) with an accelerating voltage of 15 kV, a beam current of 10 nA, and a broad beam of 30 μm. The uncertainties in melt compositions come from the inhomogeneity of the quenched products and the reaction of the sample with capsule materials and density markers, which also changes the oxidation state of the melts. The small standard deviations of the EPMA measurements (about 1% for the totals, Table 3) indicate that the quenched melts are rather homogeneous under

Table 3
Composition of run products for sink/float experiments by EPMA analysis.

Sample	Run no.	# of analyses	SiO_2 (1σ)	Al_2O_3 (1σ)	FeO^* (1σ)	MgO (1σ)	CaO (1σ)	Total (1σ)
s3	K817	19	36.8	3.6	14.2	29.6	12.9	97.2
			(0.6)	(0.2)	(0.4)	(0.8)	(0.5)	(0.6)
	K813	20	38.0	3.5	14.4	29.2	13.6	98.7
			(0.7)	(0.1)	(0.4)	(0.9)	(0.2)	(0.6)
	Average		37.4	3.6	14.3	29.4	13.2	97.9
s7	K710	18	36.8	3.6	19.0	28.2	11.9	99.5
			(0.5)	(0.2)	(0.4)	(0.9)	(0.3)	(0.9)
	K721	20	36.9	3.6	18.6	26.5	12.8	98.4
			(0.5)	(0.1)	(0.4)	(0.6)	(0.3)	(0.6)
	Average		36.9	3.6	18.8	27.3	12.4	98.9
s7_2	K959	20	35.5	3.3	18.6	25.8	11.5	94.7
			(0.4)	(0.1)	(0.5)	(0.5)	(0.4)	(0.6)
	K734	20	34.8	3.2	19.1	25.2	11.6	93.9
			(1.0)	(0.1)	(0.6)	(0.5)	(0.5)	(0.9)
	K739	20	36.2	3.3	19.3	25.4	11.4	95.6
			(0.6)	(0.1)	(0.6)	(0.7)	(0.7)	(1.0)
	Average		35.5	3.3	19.0	25.5	11.5	94.7
s6	K818	20	35.1	3.1	23.2	24.9	11.1	97.4
			(0.3)	(0.2)	(0.4)	(0.5)	(0.3)	(0.7)
	K834	20	36.0	3.5	24.5	24.6	10.6	99.1
			(0.5)	(0.1)	(0.4)	(0.7)	(0.2)	(1.1)
	K847	18	36.4	3.7	24.4	25.2	10.3	100.0
			(0.3)	(0.1)	(0.5)	(0.5)	(0.2)	(0.7)
	Average		35.9	3.4	24.0	24.9	10.7	98.8
s6_3	K680	20	34.8	3.2	23.4	22.9	10.8	95.0
			(0.7)	(0.2)	(0.5)	(0.5)	(0.4)	(0.7)
	K677	20	35.3	3.2	21.7	23.0	10.8	94.0
			(0.5)	(0.1)	(0.8)	(0.5)	(0.3)	(0.9)
	K671	20	34.5	3.1	24.6	22.3	10.5	94.9
			(0.6)	(0.1)	(0.6)	(0.7)	(0.6)	(0.5)
	Average		34.8	3.14	23.2	22.7	10.7	94.6
s6_5	K485	12	33.9	3.0	24.8	22.4	9.9	94.0
			(0.9)	(0.2)	(0.8)	(1.0)	(1.1)	(0.9)
	K460	20	35.0	3.2	23.9	23.0	9.8	94.9
			(1.1)	(0.1)	(0.9)	(0.6)	(0.7)	(1.2)
	Average		34.5	3.1	24.4	22.7	9.9	94.4
s6_7	K958	18	33.9	3.2	23.7	22.3	9.7	92.8
			(0.7)	(0.1)	(0.9)	(0.3)	(0.3)	(1.2)
	K756	21	34.2	3.2	23.5	22.1	9.4	92.3
			(0.6)	(0.1)	(0.8)	(0.4)	(0.5)	(0.9)
	K960	18	33.7	3.2	23.5	22.0	10.3	92.6
			(0.7)	(0.1)	(0.8)	(0.3)	(0.6)	(0.9)
	K727	20	33.0	3.0	23.8	20.7	9.5	89.9
			(0.9)	(0.1)	(1.0)	(0.4)	(0.5)	(1.0)
	K963	19	33.9	3.2	24.0	22.3	9.5	92.9
			(1.5)	(0.1)	(1.3)	(0.6)	(1.0)	(1.2)
	Average		33.7	3.2	23.7	21.9	9.7	92.1

Compositions are in weight percent. FeO^* represents total iron. Average compositions were used for the data analysis for equation of state.

the broad beam (30 μm diameter). After experiments on dry melts, no reaction was observed between the melts and the diamond markers nor with diamond capsules (transformed from graphite capsules at high pressures), as evidenced by the perfectly faceted shape of the single crystal diamonds in Fig. 3a. Therefore the oxidation state of the melts was likely controlled by the starting compositions. For experiments on hydrous melts, we analyzed the run product of K959 using EPMA and obtained a ReO_2 content of 0.4 wt.% with a standard deviation of 0.2 wt.%. The effect of this amount of ReO_2 on density is smaller than the typical uncertainties in the sink/float experiments (about 0.5–2.0%). We thus consider the reaction between the Re capsules and hydrous melts to be negligible. Other studies on hydrous peridotite melts using Re capsules such as Sakamaki et al. (2009) also confirmed the minimal reaction

between Re and hydrous melts. On the other hand a small degree of reaction between the melts and diamond markers can be observed (compare the shape of diamonds in Fig. 3a and b). Therefore the oxygen fugacity is likely controlled by the reaction between the melts and the diamond markers instead of the Re capsule. As shown in the Appendix, the total mass of diamond that was dissolved in the melts was so small that the oxidation state of the melts would not be affected much. Therefore the changes in melt compositions are negligible for the density measurements and the EOS fitting. The results of the EPMA analysis (Table 3) were used for the compositions of melts in our data analysis.

3.3. Preservation of water during the experiments

The starting material and run product of the test experiment (K965) on a hydrous albite melt were measured for water content using FT-IR. The FT-IR spectrum of the starting material (run product of K347) normalized by the thickness of the sample is shown in Fig. 5, which has one peak around 4480 cm^{-1} corresponding to the OH stretching mode, and a peak around 5215 cm^{-1} corresponding to the bending and stretching of H–O–H (Silver and Stolper, 1989). The total water content in the hydrous glass calculated based on the calibration of Silver and Stolper (1989) is about 8.3 wt.%. The FT-IR measurement of the run product of K965 was compared with that of the starting material in Fig. 5. The spectrum of the run product is very similar to the starting material and the calculated water content is about 7.6 wt.%, which means the water losses during experiments at such conditions are less than 9% of the water content. This observation serves as independent evidence that the Pt capsules are suitable for the preservation of water to at least 5 GPa and 2073 K.

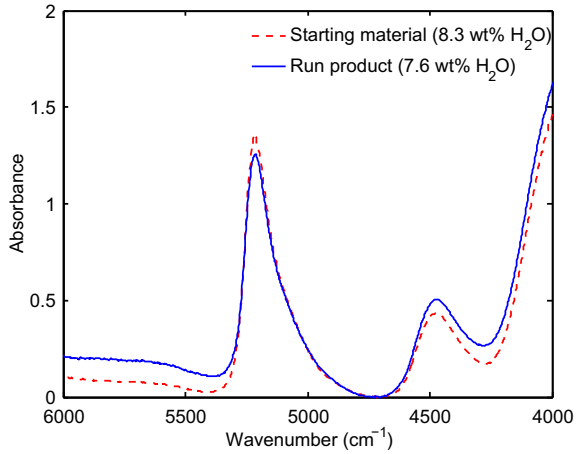

Fig. 5. FT-IR measurements for the preservation of water. The dashed curve shows the IR spectrum for the starting material of Run K965 (synthesized by Run K347). The solid curve shows the IR spectrum for the run product of K965. The IR spectra are normalized by the thickness of the samples.

For the unquenchable samples in our density measurements, the preservation of water may be evidenced (at least to some extent) by the deficit of the totals to 100% in microprobe analysis. For hydrous melts in this study, the deficits from 100% are ~4–6 wt.% for melts with a nominal H_2O content of 2 wt.%, ~5–6 wt.% for melts with 3 wt.% H_2O, ~5–6 wt.% for melts with 5 wt.% H_2O, and about ~7–10 wt.% for melts with 7 wt.% H_2O (Table 3). Note that small deficits (up to 2.8%) in totals were also observed for the anhydrous samples such as K817 and K818. This may be explained by the cracks in the recovered samples formed during decompression (see Fig. 3a). Some smaller cracks may be covered by the broad beam during the EPMA analysis and thus contribute to the small deficits in totals of the anhydrous experiments. As a comparison, the EPMA deficits for the starting material (K347) and run product (K965) of the test experiment were measured to be 10.6 and 9.9 wt.%, respectively (Table 4). These deficits are slightly larger than the water content from the FT-IR measurements (8.3 and 7.6 wt.%, respectively), similar to other unquenchable samples which also have higher deficits than the nominal water contents. The systematic correlation between the deficits and water contents gives some hint that water was retained in the melts during the experiments. However this measurement cannot serve as a quantitative observation for water contents in the melts. The reasons for this include the fact that (1) results of EPMA measurements depend on the corrections for X-ray absorption that depend on the poorly constrained density of samples; (2) water may exsolve from the melts during quenching and be lost when the sample capsules are opened for polishing; (3) the oxidation state of the melts may affect the deficits. In addition to the EPMA deficits, another line of reasoning for the retention of water may be made based upon the consideration of the limited reaction between diamonds and water. This approach is discussed in the Appendix.

4. EQUATION OF STATE FOR HYDROUS SILICATE MELTS

The equation of state for hydrous silicate melts can be determined using the measured melt densities at high pressure. In this section, we employ both the Birch–Murnaghan EOS and a new equation of state developed in Jing and

Table 4
Composition of starting material and run product for the test experiment at 5 GPa by EPMA analysis and water content by FT-IR measurements.

Run no.	# of analyses	SiO_2 (1σ)	Al_2O_3 (1σ)	Na_2O (1σ)	PtO (1σ)	Total (1σ)	H_2O (FT-IR)
K347	9	62.3 (0.7)	16.8 (0.3)	10.1 (0.2)	0.1 (0.2)	89.4 (0.8)	8.3
K965	9	62.2 (0.6)	17.4 (0.4)	10.3 (0.3)	0.2 (0.2)	90.1 (1.0)	7.6

Compositions are in weight percent.

Table 5
Parameters calculated for the Birch–Murnaghan equation of state.

Composition	P (GPa)	T (K)	ρ (g/cm^3)	ρ_0 (g/cm^3)	K_{T_0} (GPa)	K'_{T_0}
s3	14.6	2473	3.52 ± 0.01	2.70 ± 0.04	18.7 ± 3.1	9.0 ± 2.3
s7	12.9	2398	3.51 ± 0.02	2.77 ± 0.04	18.8 ± 2.9	9.2 ± 2.8
s6	10.5	2473	3.49 ± 0.02	2.81 ± 0.04	17.6 ± 2.6	10.7 ± 3.4
s7_2	14.3	2173	3.54 ± 0.02	2.63 ± 0.04	18.4 ± 2.1	6.5 ± 1.3
s6_3	10.0	2173	3.51 ± 0.03	2.57 ± 0.05	17.1 ± 1.8	4.0 ± 0.9
s6_5	11.8	2173	3.52 ± 0.03	2.39 ± 0.06	15.6 ± 1.6	3.5 ± 0.6
s6_7	13.7	2173	3.54 ± 0.07	2.23 ± 0.07	14.6 ± 1.6	3.3 ± 0.5

Uncertainties in P and T were estimated to be about 0.5 GPa and 100 K, respectively. Uncertainties in ρ_0 and K_{T_0} were estimated by propagating the uncertainties in the partial molar quantities and the uncertainties in the temperature and composition measurements. Uncertainties in ρ were estimated from the upper and lower bounds defined by the sinking and flotation of diamonds. Uncertainties in K'_{T_0} were estimated by propagating the errors from P, ρ_0, K_{T_0}, and ρ.

Karato (2011) to examine the effect of water on melt density.

4.1. Birch–Murnaghan EOS

As shown in Eq. (1), the third-order Birch–Murnaghan EOS has three parameters, the room-pressure density (ρ_0), the room-pressure bulk modulus (K_{T_0}), and the pressure derivative of bulk modulus at room pressure (K'_{T_0}). These parameters are temperature and composition dependent. Using the ideal mixing model, ρ_0 and K_{T0} can be expressed as a function of partial molar quantities, viz.,

$$\rho_0 = \frac{\sum_i X_i M_i}{\sum_i X_i \overline{V}_{0i}}, \tag{2}$$

$$K_{T_0} = -\frac{\sum_i X_i \overline{V}_{0i}}{\sum_i X_i \frac{\partial \overline{V}_i}{\partial P}}, \tag{3}$$

where M_i, $\overline{V}_{0i}$, and $\partial \overline{V}_i/\partial P$ are the molar mass, the partial molar volume, and the pressure dependence of the partial molar volume of the i-th melt component. The partial molar quantities including $\overline{V}_{0i}$ and $\partial \overline{V}_i/\partial P$ and their temperature derivatives $\partial \overline{V}_i/\partial T$ and $\partial^2 \overline{V}_i/\partial T \partial P$ have been calibrated by many studies. For components other than FeO and H_2O, we use the results of Lange (1997) and Lange and Carmichael (1987) for the partial molar volumes and their pressure dependencies, respectively. We use the results of Kress and Carmichael (1991) for the FeO component, and Ochs and Lange (1997) for the H_2O component. Uncertainties in ρ_0 and K_{T_0} can be estimated by propagating the uncertainties in the calibrated partial molar quantities (reported in the references cited above) and the uncertainties from temperature and melt composition measurements. The estimated values of ρ_0 and K_{T_0} and their uncertainties are shown in Table 5. It should be noted that there are some discrepancies between different studies on the thermal expansivities of melts at high temperatures (e.g., Toplis and Richet, 2000), which may introduce additional uncertainties. Also the partial molar volume of H_2O was determined using density data on a rather narrow range of melt compositions. Using the same value for ultramafic melts needs further verification when more experimental data become available.

Unlike the room-pressure density (ρ_0) and the room-pressure bulk modulus (K_{T_0}), the compositional dependence for the pressure derivative of bulk modulus (K'_{T_0}) is not known. Essentially, this is because the Birch–Murnaghan EOS is not based on the physics of silicate liquids and hence can only be applied to liquids empirically. An ideal mixing model for K'_{T_0} is unlikely to be justified since it relates to the second order derivative of density. As a result, an individual K'_{T_0} must be determined for each melt composition by fitting Eq. (1) using high-pressure density data and no prediction can be made for a melt with no density measurements at high pressures. The calculated K'_{T_0} for the melt compositions in this study are listed in Table 5. The uncertainties in K'_{T_0} can be estimated by propagating errors from pressure (P), ρ_0, K_{T_0}, and high pressure melt density (ρ) using the method described in Jing and Karato (2008). The estimated uncertainties in K'_{T_0} (also listed in Table 5) are quite large (about 20–30%) since we only have one density point for each melt composition.

Fig. 6a shows the calculated compression curves for the melt compositions with an Mg# of 61 including s6, s6_3, s6_5, and s6_7 using all EOS parameters in Table 5. As a result of the much smaller K'_{T_0} calculated for the hydrous melts compared to that of the anhydrous melts, the hydrous melts are so compressible at high pressure that the density for the hydrous melts becomes higher than that of the anhydrous melts at pressures higher than 17 GPa (Fig. 6a). This prediction is not consistent with the experimental observations that water reduces the density of basaltic melts at 17 and 20 GPa (Sakamaki et al., 2006), and is likely due to the large uncertainty in K_{T_0} estimated using the ideal mixing model (Ochs and Lange, 1999) based on a rather narrow range of melt compositions and due to the fact that only one density point at high pressure was used to constrain K'_{T_0}. Without obtaining more data for each melt composition, this problem cannot be resolved by the Birch–Murnaghan EOS since density data for various compositions cannot be utilized together to obtain a single unified EOS for all melt compositions.

4.2. EOS based on the model of hard sphere mixtures

A new equation of state was proposed by Jing and Karato (2011) based on the model of hard sphere mixtures (hereafter referred to as the hard-sphere EOS, although in this study the hard sphere model was modified to account for the internal energy contribution to compression and the

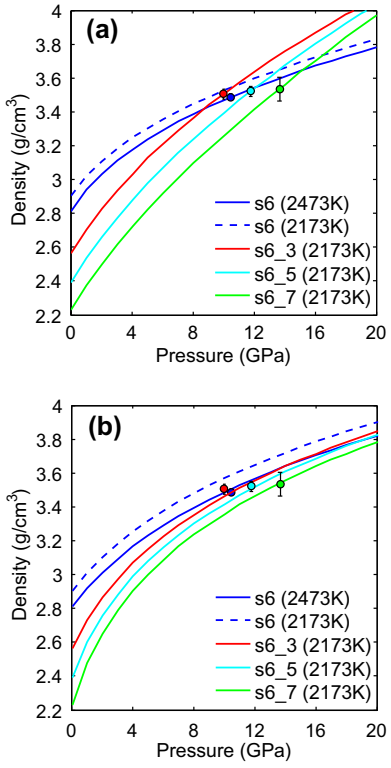

Fig. 6. Calculated compression curves for the ultramafic melts s6, s6_3, s6_5, and s6_7 using (a) Birch–Murnaghan EOS and (b) the modified hard sphere EOS. Circles represent the experimental results from sink/float experiments. Error bars represent 1% uncertainties in density.

spheres are assumed to be deformable). In this model, the melt components are considered as spheres, which constantly move in a uniform negative background potential (a liquid analogy of the Madelung energy of solids) as far as they do not overlap. Therefore, the contribution of entropy to compression is emphasized in addition to the internal energy contribution, whereas the Birch–Murnaghan equation of state mainly considers the contribution from internal energy. The deformability of spheres was introduced to explain the high-pressure density data. Detailed discussion on the formulations of the equation of state is presented in Jing and Karato (2011). The equation of state takes the form of

$$P = \frac{RT}{\overline{V}}\left[(1-\xi)\Phi - \Phi_0\left(\frac{\overline{V}_0}{\overline{V}}\right)^{\mu-1} + \xi\Phi_0\left(\frac{\overline{V}_{m0}}{\overline{V}_m}\right)^{\nu-1}\right], \quad (4)$$

where R is the gas constant; T is temperature; $\overline{V}$ is the molar volume of the melt. $\overline{V}_m = \frac{N_A\pi}{6}\sum_{i=1}^{m} X_i\sigma_i^3$ is the volume of a mole of spheres, where N_A is Avogadro's constant, X_i and σ_i are the concentration and sphere diameter of the i-th melt component. The subscript "0" indicates that a variable is evaluated at room pressure. The three different terms on the right-hand side of Eq. (4) represent the excluded volume effect, the Coulombic attraction, and the repulsive energy contribution due to the deformability of spheres. $\mu = 4/3$ and $\nu = 8/3$ are the exponents for the attractive and repulsive terms. Φ describes the deviation of the EOS from ideal gas behavior and is a function of packing fraction ($f = \overline{V}_m/\overline{V}$), which in turn depends on the molar volume of the melt ($\overline{V}$), the composition of the melt (X_i), and the sphere diameter of each melt component (σ_i). The detailed form of Φ for hard-sphere mixtures was developed by Lebowitz (1964), Lebowitz et al. (1965), and Mansoori et al. (1971). The sphere diameter σ_i is considered to be temperature and volume dependent

$$\sigma_i = \sigma_{0,T_{\rm ref}}\left(\frac{T}{T_{\rm ref}}\right)^{\eta_i}\exp\left(\frac{\xi_i}{3}\alpha_0(T-T_{\rm ref})\right)\left(\frac{\overline{V}}{\overline{V}_0}\right)^{\xi_i/3}. \quad (5)$$

where η_i and ξ_i are the temperature and volume dependencies of the sphere diameter for the i-th component, respectively. $T_{\rm ref}$ is the reference temperature and is chosen to be 1673 K in this study. ξ is an average of the deformability of spheres and can be evaluated as

$$\xi \equiv \left(\frac{\partial \ln \overline{V}_m}{\partial \ln \overline{V}}\right)_T = \frac{1}{\overline{V}_m}\sum_{i=1}^{m} X_i\overline{V}_{mi}\xi_i. \quad (6)$$

ξ is 0 for hard sphere liquids. If $\xi = 1$, spheres will have the same bulk modulus as the entire liquid and the entropic contribution to compression will vanish. In this case, the liquid will behave like a solid.

Given the equation of state (Eq. (4)), all other compressional properties at high pressure can be calculated (see Jing and Karato (2011) for detailed examples of such calculations). The advantage of the new EOS is that it is based on a physical model of hard-sphere mixtures, therefore the compositional effect is explicitly included in the EOS in contrast to the Birch–Murnaghan EOS. This enables us to employ all available melt density data for various melt compositions at high pressures to calibrate the equation of state. In addition, room-pressure data including density and bulk modulus can also be incorporated. Taking the volume derivative of Eq. (4) and letting $P = 0$, after some manipulations one obtains,

$$K_{T_0} = \frac{RT}{\overline{V}_0}\left[(1-\xi_0)^2\Gamma_0 + (2\xi_0 + (\nu-2)\xi_0^2 - \mu)\Phi_0\right], \quad (7)$$

where $\Gamma = \partial(f\Phi)/\partial f$. Eqs. (4) and (7) were employed to calibrate the EOS parameters by Jing and Karato (2011) for the CaO–MgO–Al_2O_3–SiO_2–FeO (CMASF) five component system. In this study, we combine the room-pressure bulk modulus data for the CMASF system and the high-pressure density data for hydrous and anhydrous melts determined from high-pressure experiments to recalibrate the equation of state for a six-component system, CaO–MgO–Al_2O_3–SiO_2–FeO–H_2O (CMASFH). The room-pressure bulk modulus can be obtained by ultrasonic sound velocity measurements, viz.,

$$\frac{1}{K_{T_0}} = \frac{\overline{V}_0}{c^2} + \frac{T\overline{V}_0\alpha_0^2}{C_{P_0}}, \quad (8)$$

where c is the measured sound velocity for silicate liquids. α_0 and C_{P_0} are room-pressure values of the thermal expansivity and heat capacity of silicate liquids. $\overline{V}_0$, α_0 and C_{P_0} can be calculated by the ideal-mixing model (Lange and Carmichael, 1987; Kress and Carmichael, 1991; Lange,

1997; Ochs and Lange, 1997). Note that the majority of data used for the EOS fitting are the room-pressure sound velocity data, which were obtained at relatively low temperatures around 1673 K. At these temperatures, the room-pressure molar volumes are better constrained and the choice of different calibrations for the partial molar volumes is less critical. The same set of sound velocity data as in Jing and Karato (2011) were used for the calibration of the CMASFH system, which includes the results of Ai and Lange (2008) for the CMAS melts, the results of Webb and Courtial (1996) on two CAS compositions (Ca53.12 and Ca38.27), the results of Secco et al. (1991) on Di_{64}–An_{36}, and the results of Rivers and Carmichael (1987) on $CaMgSi_2O_6$ (Di), $CaAl_2Si_2O_8$ (An), $CaSiO_3$, Di_{50}–An_{50}, Fe_2SiO_4, and another FeO–SiO_2 composition Fs-2. Only relaxed sound velocity data are included. Velocity data that show frequency dependence or data with no frequency information are not included in the calibration. High-pressure density data are mostly from sink/float measurements except for a very recent study which employs the X-ray absorption technique (Sakamaki et al., 2009). In addition to the density data on anhydrous melts compiled in Jing and Karato (2008), we also include all available data on hydrous melts (Matsukage et al., 2005; Sakamaki et al., 2006, 2009; Agee, 2008) and the seven data points from this study.

A nonlinear regression (Regression #1) was conducted using both room-pressure bulk modulus data and high-pressure density data. The calculated sphere diameters and their temperature and volume dependencies are listed in Table 6. The sphere diameter for the H_2O component is 0.172 ± 0.007 nm at 1673 K with a temperature dependence (η_i) of 0.06 ± 0.09 and a volume dependence (ξ_i) of -0.35 ± 0.29. The parameters for other components are similar to the previous calibrations for anhydrous melts (Jing and Karato, 2011). This indicates that the addition of water has little influence on the bonding properties of other components. Fig. 7 plots the % residuals of the regression with respect to pressure. The hard sphere EOS can explain the experimental data very well. For most melt compositions, the difference between the predicted densities and the experimental results is less than 1%.

In the preceding regression, the uncertainty in the volume dependence of the sphere diameter for the H_2O component is quite high due to the limited number of density measurements on hydrous silicate melts at both low and high pressures. We therefore conducted another regression (Regression #2) by assuming that the sphere diameter for the H_2O component does not depend on volume. Regressed parameters using this model are listed in Table 7. The predicted densities at high pressure for these melts are listed in Table 8. The% residuals of the regression are shown in Fig. 7. The density can be equally well reproduced by this model although fewer parameters are employed.

Fig. 6b compares the compression curves for the melts with Mg# 61 from this study (i.e., s6, s6_3, s6_5, and s6_7) using parameters from Regression #2 (Table 7). In contrast to the Birch–Murnaghan EOS, it does not predict denser hydrous melts than the corresponding anhydrous melt at high pressure. A detailed comparison reveals that the hard-sphere EOS predicts much smaller room-pressure bulk modulus (Table 8) than the ideal mixing model (Table 5). For example, the calculated K_{T_0} for melts s6_3, s6_5, and s6_7 at 2173 K are 12.8, 9.2, and 7.0 GPa, respectively, whereas the corresponding ideal-mixing model results are 17.1, 15.6, and 14.6 GPa, respectively. Experimental studies on the bulk modulus of hydrous silicate melts at very low pressures (room pressure is impractical due to the degassing of H_2O) are needed to test these results.

Table 6
Calibrated sphere diameters and their temperature and volume dependences for melt components in the CMASFH system for Regression #1.

Component	$\sigma_{i,T_{ref}}$ (nm)	η_i	ξ_i
SiO_2	0.369 ± 0.002	-0.04 ± 0.01	0.70 ± 0.06
Al_2O_3	0.326 ± 0.006	-0.03 ± 0.02	0.58 ± 0.15
FeO	0.286 ± 0.003	0.01 ± 0.02	0.17 ± 0.08
MgO	0.272 ± 0.002	0.03 ± 0.02	0.12 ± 0.08
CaO	0.315 ± 0.003	-0.07 ± 0.02	0.09 ± 0.10
H_2O	0.172 ± 0.007	0.06 ± 0.09	-0.35 ± 0.29

Uncertainties represent one σ error estimates.

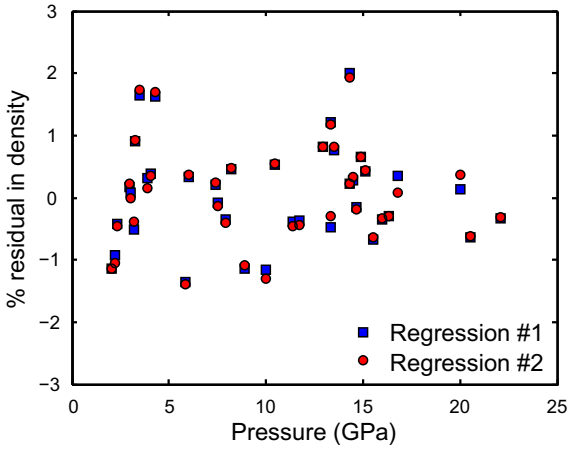

Fig. 7. Percentage residuals of density calculated from Regression #1 (squares) and Regression #2 (circles) for the melt density data in Table 8 plotted against pressure.

Table 7
Calibrated sphere diameters and their temperature and volume dependencies for melt components in the CMASFH system for Regression #2.

Component	$\sigma_{i,T_{ref}}$ (nm)	η_i	ξ_i
SiO_2	0.369 ± 0.002	-0.04 ± 0.01	0.69 ± 0.06
Al_2O_3	0.326 ± 0.006	-0.03 ± 0.02	0.58 ± 0.14
FeO	0.285 ± 0.003	0.01 ± 0.02	0.15 ± 0.09
MgO	0.272 ± 0.002	0.04 ± 0.02	0.14 ± 0.08
CaO	0.315 ± 0.003	-0.06 ± 0.02	0.07 ± 0.10
H_2O	0.180 ± 0.004	0.13 ± 0.06	—

Uncertainties represent one σ error estimates.

Table 8
High-pressure density data used for the calibration of the hard sphere EOS for hydrous silicate melts and the predictions of the EOS using the parameters in Table 7.

Composition	T (K)	P (GPa)	ρ_{Exp} (g/cm^3)	$\overline{V}_0$ (cm^3/mol)	f_0	K_{T_0} (GPa)	ρ_{Calc} (g/cm^3)	Residual (g/cm^3)	% Residual
KLB-1[a]	2273	8.2	3.210	19.13	0.54	21.9	3.225	0.015	0.5
IT8720[b]	2543	16.3	3.560	19.64	0.53	22.2	3.549	−0.011	−0.3
MA[b]	2603	16.0	3.560	19.94	0.53	21.7	3.548	−0.012	−0.3
MA[b]	2163	7.4	3.310	19.14	0.55	22.5	3.318	0.008	0.2
PHN1611[c]	2303	13.5	3.420	19.19	0.54	22.3	3.448	0.028	0.8
PHN1611[c]	2633	20.5	3.590	19.82	0.53	21.8	3.567	−0.023	−0.6
Pyrolite[c]	2633	22.1	3.600	19.92	0.53	21.6	3.589	−0.011	−0.3
Komatiite[a]	2173	8.9	3.370	19.79	0.55	20.3	3.333	−0.037	−1.1
Komatiite[a]	2073	6.0	3.190	19.62	0.55	20.4	3.202	0.012	0.4
Picritic[d]	2773	14.5	3.490	21.42	0.53	19.9	3.501	0.011	0.3
MORB[e]	1673	5.9	3.230	21.38	0.58	18.1	3.185	−0.045	−1.4
MORB[d]	2473	14.9	3.520	22.45	0.54	17.5	3.543	0.023	0.6
MORB[d]	2773	15.1	3.500	22.81	0.53	17.2	3.515	0.015	0.4
s3[f]	2473	14.6	3.523	19.53	0.53	22.8	3.516	−0.006	−0.2
s7[f]	2398	12.9	3.514	19.36	0.54	23.1	3.543	0.029	0.8
s6[f]	2473	10.5	3.487	19.48	0.53	22.7	3.506	0.019	0.5
s3-a[f]	2173	15.5	3.551	18.26	0.46	9.7	3.528	−0.023	−0.6
s7-a[f]	2173	14.3	3.542	18.27	0.46	9.5	3.549	0.008	0.2
s5-a[f]	2173	13.3	3.533	18.26	0.46	9.3	3.575	0.042	1.2
s6-a[f]	2173	11.4	3.518	18.28	0.46	9.3	3.502	−0.016	−0.5
s7_2[f]	2173	14.3	3.542	18.69	0.51	15.6	3.610	0.068	1.9
s6_3[f]	2173	10.4	3.506	18.60	0.49	12.8	3.460	−0.046	−1.3
s6_5[f]	2173	11.7	3.521	18.36	0.46	9.2	3.506	−0.015	−0.4
s6_7[f]	2173	13.3	3.536	18.21	0.43	7.0	3.526	−0.010	-0.3
MORB + 2 wt.% H_2O[g]	2573	16.8	3.550	21.88	0.51	12.9	3.553	0.003	0.1
MORB + 8 wt.% H_2O[g]	2473	20.0	3.580	20.76	0.43	5.7	3.593	0.013	0.4
$Ko_{50}Fa_{50}$ + 5 wt.% H_2O[h]	1773	2.1	3.099	17.61	0.47	8.6	3.064	−0.035	−1.1
	1773	3.0	3.188	17.61	0.47	8.6	3.195	0.007	0.2
	1773	3.5	3.207	17.61	0.47	8.6	3.262	0.055	1.7
$Ko_{50}Fa_{50}$ + 2 wt.% H_2O[h]	2023	7.5	3.645	18.77	0.51	14.2	3.640	−0.005	−0.1
	2073	7.9	3.663	18.88	0.51	14.1	3.648	−0.015	−0.4
Pyrolite + 5 wt.% H_2O[i]	1873	2.4	2.730	18.05	0.48	9.3	2.718	−0.012	−0.5
	1973	2.2	2.690	18.31	0.48	9.3	2.662	−0.028	−1.0
	1773	3.2	2.870	17.79	0.49	9.3	2.859	−0.011	−0.4
	1873	3.3	2.800	18.05	0.48	9.3	2.826	0.026	0.9
	1973	3.0	2.760	18.31	0.48	9.3	2.760	0.000	0.0
	1873	4.3	2.880	18.05	0.48	9.3	2.929	0.049	1.7
	1973	4.1	2.860	18.31	0.48	9.3	2.870	0.010	0.4
	2073	3.9	2.810	18.57	0.48	9.2	2.814	0.004	0.2

ρ_{Exp} is from high-pressure experiments. $\overline{V}_0$ is calculated from the ideal-mixing model. f_0, K_{T_0}, and ρ_{Calc} are calculated from the hard sphere EOS using the parameters in Table 6. Data sources: [a]Agee and Walker (1993); [b]Suzuki et al. (1998); [c]Suzuki and Ohtani (2003); [d]Ohtani and Maeda (2001); [e]Agee (1998); [f]This study; [g]sakamaki et al. (2006); [h]Agee (2008); [i]Sakamaki et al. (2009).

4.3. Effect of H_2O on melt density

In order to evaluate the effect of water on melt density at high pressures, we apply the hard sphere EOS to melts by mixing an anhydrous melt composition with various amounts of water. As an example, we choose the dry melt composition as 35.7 wt.% SiO_2, 3.3 wt.% Al_2O_3, 21.9 wt.% FeO, 24.8 wt.% MgO, and 14.3 wt.% CaO, which represents the dry part of a likely mantle melt at the bottom of the upper mantle studied in Jing and Karato (2009) (hereafter referred to as the Dry Mantle Melt composition). Using the parameters obtained from both Regression #1 and Regression #2 (Table 6 and Table 7), the densities of the melt as a function of water content are calculated at 14 GPa and 2173 K and are shown in Fig. 8. The results of two regression models are almost identical when water content is smaller then 5 wt.%. The difference in the predicted density between the two models is only 0.6% at 10 wt.% water content, and is less than 3% at 20 wt.%. The effect of water on density is large. By adding 5 wt.%

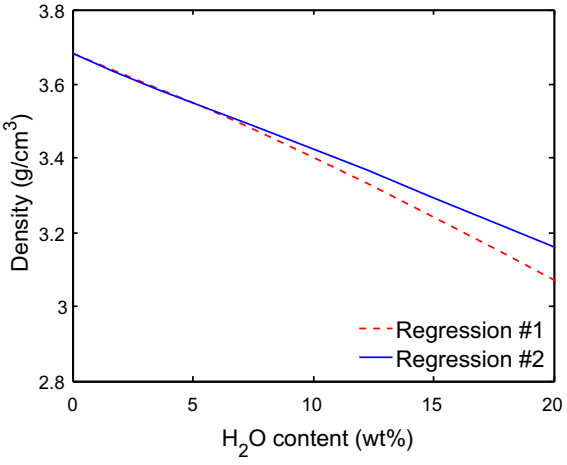

Fig. 8. Density of hydrous silicate melts as a function of water content at 14 GPa and 2173 K.

(~0.14 in mole fraction) water, the density of this melt decreases from 3.68 to 3.55 g/cm^3.

According to the hard sphere EOS, the influence of composition on melt density is controlled by three factors, the molecular mass, the partial molar volume, and the sphere diameter of the component. For the H_2O component, it has a very small molecular mass, a relatively large partial molar volume at room pressure, and a very small sphere diameter. The small molecular mass makes the H_2O component a very light component, and hence is the main reason that water can reduce the melt density dramatically at room pressure. On the other hand, the small sphere diameter of H_2O makes the packing fraction of the hydrous silicate melts significantly smaller than that of the anhydrous melts. For example, by adding 3, 5, and 7 wt.% H_2O, the packing fraction of the s6 melt decreases from 0.53 to 0.49, 0.46, and 0.43, respectively (Table 8). It has been shown in Jing and Karato (2011) that, for hard sphere liquids, the bulk modulus is a monotonically increasing function of the packing fraction as the compression of liquids is mainly controlled by the change in entropy (or excluded volume), but not the internal energy of the liquid. Therefore the small bulk modulus for the hydrous melts is likely a direct consequence of the small sphere size of the H_2O component, which means a small excluded volume or a small packing fraction. The small bulk modulus of the hydrous melts indicates that at high pressure the effect of H_2O on melt density is less significant compared to that at low pressure.

5. CONDITIONS FOR DENSITY CROSSOVERS AT THE BOTTOM OF THE UPPER MANTLE

It is hypothesized in the transition-zone water-filter model (Bercovici and Karato, 2003; Karato et al., 2006) that the melt formed by water-assisted melting may be denser than the upper mantle minerals (but lighter than the transition zone minerals). Our previous study (Jing and Karato, 2009) tested this dense melt hypothesis for various melt compositions and concluded that for a melt that coexists with a pyrolite mantle, the conditions for density crossovers between the melt and the solid mantle at 410 km depth are marginally satisfied. However, the uncertainty of that calculation was rather large due to the uncertainties in the partial molar volume of H_2O at 14 GPa (8 ± 2 cm^3/mol) (Matsukage et al., 2005). With more density data on hydrous melts including the results of this study and the equation of state we have developed, it becomes possible to better constrain the conditions for density crossovers at 410 km depth.

The composition of the melt formed at the conditions of the bottom of the upper mantle is not well constrained. However, according to the analysis of Jing and Karato (2009), FeO and H_2O are the most important components that control melt density under such conditions. We therefore start from the Dry Mantle Melt composition in Jing and Karato (2009). The partitioning of Mg and Fe between melts and minerals can be described by the distribution coefficient $K_D = (X_{FeO}/X_{MgO})^{olivine}/(X_{FeO}/X_{MgO})^{melt}$, which was estimated to be about 0.25 at the 410 km depth from the most recent experimental data by Mibe et al. (2006). Using this distribution coefficient (K_D) and assuming the melt is in equilibrium with a pyrolite mantle (Mg# is 89), the Mg# of the Dry Mantle Melt is estimated to be 67. The addition of water may affect the distribution of Mg and Fe between melts and minerals. However, the experimental results of Kawamoto and Holloway (1997) on the melting of water saturated peridotite showed a similar K_D (about 0.258) at 11 GPa. We therefore consider the effect of water on Fe/Mg partitioning to be negligible and choose 67 as the Mg# for the melt formed at 410 km depth. The complete discussion on the effect of Mg# on melt density was presented in Jing and Karato (2009).

We apply the hard sphere equation of state to the Dry Mantle Melt + H_2O system to constrain the conditions at which melts are denser than solids at 410 km depth. The critical water content at which the hydrous melts have the same density as the upper mantle materials at 14 GPa can be defined. The critical water content is then a function of temperature due to the large difference in the thermal expansivities of melts and solids. At a higher temperature, the density of the melt would decrease significantly due to the high thermal expansivity of the melt whereas the density of the solid mantle would not decrease as much. Therefore the critical water content will be lower at higher temperatures. The critical water content can be obtained by solving the following equation

$$\rho^{melt}(T, X_{H_2O}) = \rho^{solid}_{T_s} \exp[-\alpha^{solid}(T - T_s)], \quad (9)$$

where T_s is the reference temperature at which the density of the solid mantle $\rho^{solid}_{T_s}$ is determined; α^{solid} is the thermal expansivity of the solid at 14 GPa. $\rho^{solid}_{T_s}$ is 3.54 g/cm^3 from the PREM model (Dziewonski and Anderson, 1981) with a reference temperature (T_s) of 1800 K. α^{solid} can be estimated from the thermodynamic relation of $\alpha/\alpha_0 = (\rho/\rho_0)^{-\delta_T}$. If $\alpha_0 = 3 \times 10^{-5} K^{-1}$, $\rho_0 = 3.3$g/cm^3, and the Anderson–Grüneisen parameter $\delta_T = 5.5$ (Fei, 1995), then $\alpha^{solid} = 2.1 \times 10^{-5} K^{-1}$. The calculation is similar to that in Jing and Karato (2009), but the density of hydrous melts is calculated in a self-consistent manner from the hard

sphere equation of state directly instead of assuming the ideal mixing model with a constant partial molar volume and a poorly constrained thermal expansivity for hydrous melts at 14 GPa.

The calculated critical water content for density crossover as a function of temperature is presented in Fig. 9. Predictions of both regression models are plotted to show the possible range of uncertainty. As expected, the critical water content decreases with increasing temperature. The calculated critical water content is similar to that of Jing and Karato (2009) as shown in Fig. 9. It is interesting to compare the critical water content with the water content in a melt formed at 410-km, which is also a function of temperature. The water content in the melts is controlled by the melting relations of the silicate–H_2O system (i.e. the liquidus of the silicate–H_2O system). However, the liquidus is not well determined due to the experimental difficulty of measuring water content in unquenchable melts. The range of liquidus (shown as the blue-shaded area in Fig. 9) was summarized by Jing and Karato (2009) based on the melting experiments of (Inoue, 1994; Litasov and Ohtani, 2002, 2003). At the likely mantle temperature of 1800–2000 K at 410 km depth (shown as the yellow-shaded area in Fig. 9), the water content in the melt that coexists with a pyrolite mantle is about 10–15 wt.%, which is close to the critical water content at such temperatures. Therefore the conclusion is similar to that of Jing and Karato (2009), that is, the conditions for a negatively buoyant melt at the bottom of the upper mantle are marginally satisfied if water is the only volatile component in the system.

However, this conclusion needs to be modified if other volatile components such as CO_2, K_2O N_2O are present. All of these components help melting and are denser than H_2O. Consequently, the water content of the melt formed at 410-km will be lower if these components exist, and the melt density will be higher. A preliminary analysis was given using a conventional model of liquids by Karato et al. (2006). A similar analysis will be needed where a hard-sphere EOS is used, but the hard-sphere parameters for these components have not been determined.

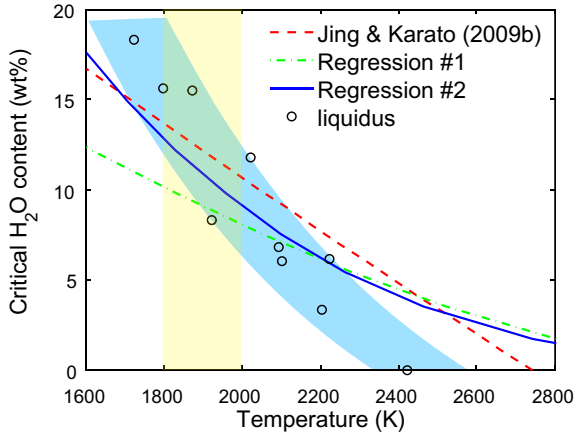

Fig. 9. Critical water content as a function of temperature for density crossover at 410 km depth. The liquidus of the peridotite–H_2O pseudo-binary system is shown as circles and the blue shaded area. The yellow shaded area indicates the possible temperature range at 410 km depth. (For interpretation of the references to colour in this figure legend, the reader is referred to the web version of this article.)

6. CONCLUSIONS

Sink/float experiments were conducted to determine the density of three anhydrous melts and four hydrous melts. A new equation of state based on the model of hard sphere mixtures was calibrated using both room-pressure bulk modulus and high-pressure density data. The effect of water on melt density at high pressure was then constrained using this equation of state. The small molecular mass of the H_2O component reduces the density of hydrous melts, whereas the small sphere diameter of H_2O makes the melts more compressible and the effect of water on melt density less significant at high pressures. The critical conditions for density crossovers between the hydrous melts and the upper mantle at the 410 km boundary were constrained. By comparing the critical water content with melting relations for the peridotite–H_2O system, we conclude that the hydrous melts can be as dense as the upper mantle minerals at 410 km depth depending on the temperature and Mg# of the mantle.

ACKNOWLEDGEMENTS

This work was supported by the National Science Foundation. We thank K. Matsukage and T. Kawazoe for their help on high-pressure experiments, Z. Jiang for SEM analysis, J.O. Eckert Jr. for EPMA analysis, and H. Sumiya for the supply of diamond single crystals. Constructive reviews by P. Asimow, P. Richet, an anonymous reviewer, and Associate Editor M. Toplis have significantly improved the manuscript.

APPENDIX A. PRESERVATION OF WATER AND THE OXIDATION STATE OF MELTS

Water loss occurs mostly through hydrogen diffusion associated with the decomposition of water as,

$$H_2O(\text{melt}) = H_2(\text{fluid}) + \frac{1}{2}O_2(\text{fluid}). \quad \text{(A1)}$$

Consequently, the loss of water accompanies an increase in oxygen fugacity of the melts. In order to maintain the mass balance and the charge balance, the leftover oxygen from hydrogen diffusion must be consumed by both the oxidation of diamonds and the oxidation of ferrous iron to ferric iron in the melts.

$$C(\text{diamond}) + O_2 + O^{2-}(\text{melt}) = CO_3^{2-}(\text{melt}) \quad \text{(A2)}$$

$$4FeO(\text{melt}) + O_2 = 2Fe_2O_3(\text{melt}) \quad \text{(A3)}$$

Note that the melts in this study have low SiO_2 and Al_2O_3 contents and therefore are depolymerized (Mysen, 1990). Therefore the speciation of dissolved CO_2 will most likely be in the form of carbonates (Brooker et al., 2001). Similar processes have been discussed by Holloway et al. (1992) for their melting experiments in the presence of graphite capsule. Following their approach, the ferric/ferrous ratio and the amount of CO_2 dissolved in the melt can be obtained as functions of oxygen fugacity. The thermodynamic equilibrium of reaction (A2) can be described as

$$X_{CO_3^{2-}} = K_1 X_{O^{2-}} f_{O_2}, \quad (A4)$$

with the mole fraction of O^{2-} being calculated as

$$X_{O^{2-}(melt)} = 1 - X_{CO_3^{2-}(melt)}. \quad (A5)$$

Then the mole fraction of CO_3^{2-} is

$$X_{CO_3^{2-}}(melt) = \frac{K_1 f_{O_2}}{1 + K_1 f_{O_2}}. \quad (A6)$$

The equilibrium constant K_1 as a function of temperature and pressure can be found in Holloway et al. (1992). For the iron redox reaction (A3), we apply the model of Kress and Carmichael (1991) to obtain the ferric/ferrous ratio in the melt.

Here we use melt s6_7 as an example to calculate the water loss during the experiments. Fig. A1a shows the relation between the dissolved CO_2 in the melt s6_7 and the oxygen fugacity of the melt at 14 GPa and 2173 K. The calculated FeO and Fe_2O_3 contents as functions of oxygen fugacity are shown in Fig. A1b. Combining Fig. A1a and b, if the amount of CO_3^{2-} in the melt is known, then the FeO and Fe_2O_3 contents in the melt can be obtained assuming the oxygen fugacity is homogeneous everywhere in the melt. Therefore the finial composition of the melt can be inferred from the amount of diamonds dissolved in the melt. By comparing with the initial composition of the melt, the amount of water reacted with diamond and that reacted with FeO can be obtained. Then the total loss of water is given by the sum of these two. The CO_3^{2-} content in the starting melt is simply zero. We estimate the initial contents of FeO and Fe_2O_3 using an oxygen fugacity of 2 orders of magnitude lower than the Ni–NiO buffer, at which the starting materials were synthesized. Fig. A2 shows the calculated water loss in wt.% of the melt as a function of dissolved CO_2 in the melt. It can be seen that the dissolution of diamonds plays a major role in consuming the oxygen that is dissociated from H_2O.

The amount of diamond dissolved into the melts can be estimated based on the size change of diamonds after experiments. In most hydrous experiments conducted on composition s6_7, the diamond diameter decreased from 120 to 100 μm. If four diamond markers were loaded in the capsule, then about 5.3×10^{-9} kg of diamond would dissolve into the melt. The size of the sample is about 1 mm in diameter and 2 mm long, then the mass of the melt is about 5.5×10^{-6} kg assuming a density of 3.5 g/cm^3 at 14 GPa. Therefore after experiments, the melt contained about 0.4 wt.% CO_2. This amount of CO_2 indicates a $\log_{10} fO_2$ of about 0.8 $\log_{10}$ units lower than the Ni–NiO oxide buffer (Fig. A1a). From Fig. A1b, about 1 wt.% of the melt will be oxidized from FeO to Fe_2O_3. The estimate water loss is about 0.4 wt.%, and about 6% of the total water in the melt (Fig. A2). Consequently, the limited dissolution of the diamond markers will only cause a small density change that is much less than the typical uncertainty (about 1%) in sink/float measurements.

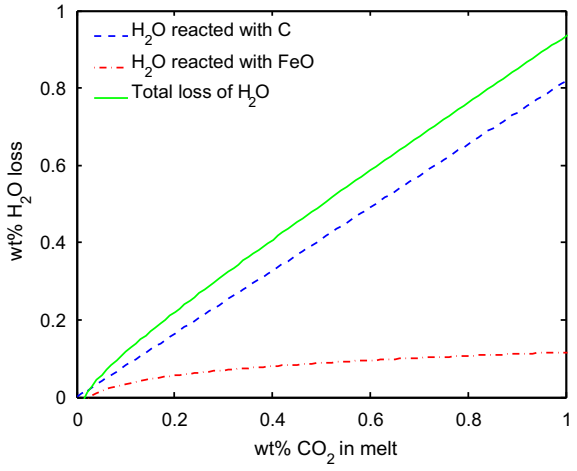

Fig. A2. The relation of water loss with the amount of CO_2 dissolved in the melt.

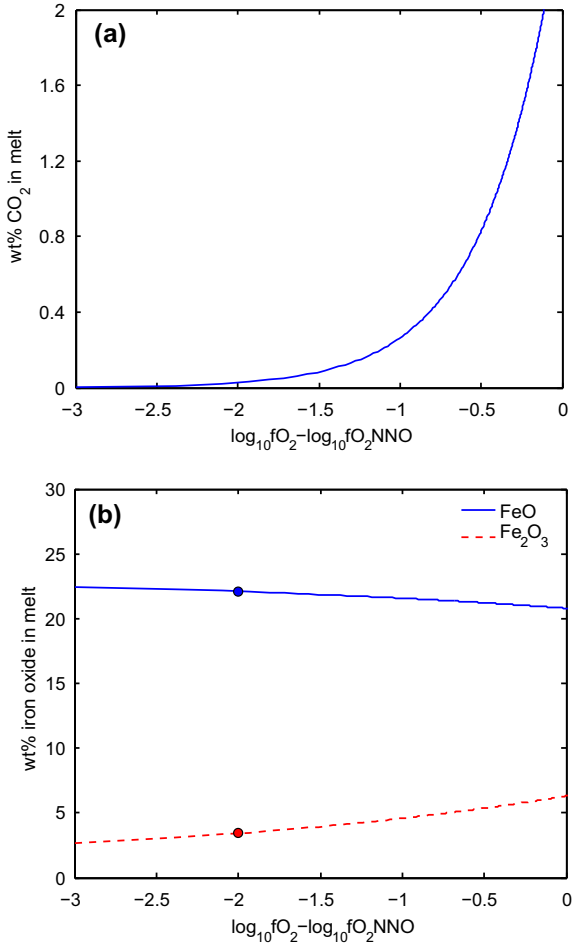

Fig. A1. The relations between fO_2 and dissolved CO_2, ferric iron, and ferrous iron in s6_7 melt at 14 GPa and 2173 K. (a) Weight percent CO_2 in the melt; (b) weight percent FeO (solid blue curve) and Fe_2O_3 (red dashed curve) in the melt. Symbols indicate the initial contents at an fO_2 of 2 $\log_{10}$ units lower than the Ni–NiO buffer. (For interpretation of the references to colour in this figure legend, the reader is referred to the web version of this article.)

REFERENCES

Agee C. B. (1998) Crystal–liquid density inversions in terrestrial and lunar magmas. *Phys. Earth Planet. In.* **107**, 63–74.

Agee C. B. (2008) Static compression of hydrous silicate melt and the effect of water on planetary differentiation. *Earth Planet. Sci. Lett.* **265**, 641–654.

Agee C. B. and Walker D. (1988) Static compression and olivine flotation in ultrabasic silicate liquid. *J. Geophys. Res.* **93**(B4), 3437–3449.

Agee C. B. and Walker D. (1993) Olivin flotation in mantle melt. *Earth Planet. Sci. Lett.* **114**, 315–324.

Ai Y. and Lange R. A. (2008) New acoustic velocity measurements on CaO–MgO–Al_2O_3–SiO_2 liquids: reevaluation of the volume and compressibility of $CaMgSi_2O_6$–$CaAl_2Si_2O_8$ liquids to 25 GPa. *J. Geophys. Res.* **113**, B04203.

Bercovici D. and Karato S. (2003) Whole-mantle convection and the transition-zone water filter. *Nature* **425**, 39–44.

Brooker R. A., Kohn S. C., Holloway J. R. and McMillan P. F. (2001) Structural controls on the solubility of CO_2 in silicate melts Part II: IR characteristics of carbonate groups in silicate glasses. *Chem. Geol.* **174**, 241–254.

Burnham C. W. and Davis N. F. (1971) The role of H_2O in silicate melts I. P–V–T relations in the system $NaAlSi_3O_8$–H_2O to 10 kilobars and 1000 °C. *Am. J. Sci.* **270**, 54–79.

Dingwell D. B., Courtial P., Giordano D. and Nichols A. R. L. (2004) Viscosity of peridotite liquid. *Earth Planet. Sci. Lett.* **226**, 127–138.

Dziewonski A. M. and Anderson D. L. (1981) Preliminary reference Earth model. *Phys. Earth Planet. In.* **25**, 297–356.

Fei Y. (1995) Thermal expansion. In *Mineral Physics & Crystallography: A Handbook Of Physical Constants* (ed. T. J. Ahrens). American Geophysical Union, Washington, D.C., pp. 29–41.

Holloway J. R., Pan V. and Gudmundsson G. (1992) High-pressure fluid-absent melting experiments in the presence of graphite: oxygen fugacity, ferric/ferrous ratio and dissolved CO_2. *Eur. J. Mineral.* **4**, 105–114.

Inoue T. (1994) Effect of water on melting phase relations and melt composition in the system Mg_2SiO_4–$MgSiO_3$–H_2O up to 15 GPa. *Phys. Earth Planet. In.* **85**, 237–263.

Inoue T. and Sawamoto H. (1992) High pressure melting of pyrolite under hydrous condition an its geophysical implications. In *High-Pressure Research: Application to Earth and Planetary Sciences* (eds. Y. Syono and M. H. Manghnani). American Geophysical Union, Washington, D.C., pp. 323–331.

Jing Z. and Karato S. (2008) Compositional effect on the pressure derivatives of bulk modulus of silicate melts. *Earth Planet. Sci. Lett.* **272**, 429–436.

Jing Z. and Karato S. (2009) The density of volatile bearing melts in the Earth's deep mantle: the role of chemical composition. *Chem. Geol.* **262**, 100–107.

Jing Z. and Karato S. (2011) A new approach to the equation of state of silicate melts: an application of the theory of hard sphere mixtures. *Geochim. Cosmochim. Acta* **75**, 6780–6802.

Karato S., Bercovici D., Leahy G., Richard G. and Jing Z. (2006) The transition-zone water filter model for global material circulation: where do we stand? In *Earth's Deep Water Cycle* (eds. S. D. Jacobsen and S. van der Lee). American Geophysical Union, Washington, D.C., pp. 289–313.

Kawamoto T. and Holloway J. R. (1997) Meting temperature and partial melt chemistry of H_2O-saturated mantle peridotite to 11 gigapascals. *Science* **276**, 240–243.

Kress V. C. and Carmichael I. S. E. (1991) The compressibility of silicate liquids containing Fe_2O_3 and the effect of composition, temperature, oxygen fugacity and pressure on their redox states. *Contrib. Mineral. Petrol.* **108**, 82–92.

Lange R. A. (1997) A revised model for the density and thermal expansivity of K_2O–Na_2O–CaO–MgO–Al_2O_3–SiO_2 liquids from 700 to 1900 K: extension to crustal magmatic temperatures. *Contrib. Mineral. Petrol.* **130**, 1–11.

Lange R. A. and Carmichael I. S. E. (1987) Densities of Na_2O–K_2O–CaO–MgO–FeO–Fe_2O_3–$A1_2O_3$–TiO_2–SiO_2 liquids: new measurements and derived partial molar properties. *Geochim. Cosmochim. Acta* **51**, 2931–2946.

Lebowitz J. L. (1964) Exact solution of generalized Percus–Yevick equation for a mixture of hard spheres. *Phys. Rev.* **133**, A895–A899.

Lebowitz J. L., Helfand E. and Praestgaard E. (1965) Scaled particle theory of fluid mixtures. *J. Chem. Phys.* **43**, 774–779.

Liebske C., Schmickler B., Terasaki H., Poe B. T., Suzuki A., Funakoshi K.-i., Ando R. and Rubie D. C. (2005) Viscosity of peridotite liquid up to 13 GPa: implications for magma ocean viscosities. *Earth Planet. Sci. Lett.* **240**, 589–604.

Litasov K. and Ohtani E. (2002) Phase relations and melt compositions in CMAS-pyrolite–H_2O system up to 25 GPa. *Phys. Earth Planet. In.* **134**, 105–127.

Litasov K. and Ohtani E. (2003) Hydrous solidus of CMAS–pyrolite and melting of mantle plumes at the bottom of the upper mantle. *Geophys. Res. Lett.* **30**(22), 2143. http://dx.doi.org/10.1029/2003GL018318.

Mansoori G. A., Carnahan N. F., Starling K. E. and Leland T. W. (1971) Equilibrium thermodynamic properties of the mixture of hard spheres. *J. Chem. Phys.* **54**, 1523–1525.

Matsukage K. N., Jing Z. and Karato S. (2005) Density of hydrous silicate melt at the conditions of Earth's deep upper mantle. *Nature* **438**, 488–491.

Mibe K., Fujii T., Yasuda A. and Ono S. (2006) Mg–Fe partitioning between olivine and ultramafic melts at high pressure. *Geochim. Cosmochim. Acta* **70**, 757–766.

Miller G. H., Stolper E. M. and Ahrens T. J. (1991) The equation of state of a molten komatiite 1. Shock wave compression to 36 GPa. *J. Geophys. Res.* **96**, 11831–11848.

Morishima H., Kato T., Suto M., Ohtani E., Urakawa S., Utsumi W., Shimomura O. and Kikegawa T. (1994) The phase boundary between α- and β-Mg2SiO4 determined by in situ X-ray observation. *Science* **265**, 1202–1203.

Mysen B. O. (1990) Relationships between silicate melt structure and petrologic processes. *Earth Sci. Rev.* **27**, 281–365.

Ochs F. A. and Lange R. A. (1997) The partial molar volume, thermal expansivity, and compressibility of H_2O in $NaAlSi_3O_8$ liquid: new measurements and an internally consistent model. *Contrib. Mineral. Petrol.* **129**, 155–165.

Ochs F. A. and Lange R. A. (1999) The density of hydrous magmatic liquids. *Science* **283**, 1314–1317.

Ohtani E. and Maeda M. (2001) Density of basaltic melt at high pressure and stability of the melt at the base of the lower mantle. *Earth Planet. Sci. Lett.* **193**, 69–75.

Ohtani E., Suzuki A. and Kato T. (1998) Flotation of olivine and diamond in mantle melt at high pressure: implications for fractionation in the deep mantle and ultradeep origin of diamond. In *Properties of Earth and Planetary Materials at High Pressure and Temperature* (eds. M. H. Manghnani and T. Yagi). American Geophysical Union, Washington, D.C., pp. 227–238.

Revenaugh J. and Sipkin S. A. (1994) Seismic evidence for silicate melt atop the 410 km mantle discontinuity. *Nature* **369**(6480), 474–476.

Rigden S. M., Ahrens T. J. and Stolper E. M. (1988) Shock compression of molten silicate: results for a model basaltic composition. *J. Geophys. Res.* **93**, 367–382.

Rigden S. M., Ahrens T. J. and Stolper E. M. (1989) High-pressure equation of state of molten anorthite and diopside. *J. Geophys. Res.* **94**, 9508–9522.

Rivers M. L. and Carmichael I. S. E. (1987) Ultrasonic studies of silicate melts. *J. Geophys. Res.* **92**(B9), 9247–9270.

Sakamaki T., Suzuki A. and Ohtani E. (2006) Stability of hydrous melt at the base of the Earth's upper mantle. *Nature* **439**, 192–194.

Sakamaki T., Ohtani E., Urakawa S., Suzuki A. and Katayama Y. (2009) Measurement of hydrous peridotite magma density at high pressure using the X-ray absorption method. *Earth Planet. Sci. Lett.* **287**, 293–297.

Secco R. A., Manghnani M. H. and Liu T.-C. (1991) The bulk modulus – attenuation – viscosity systematics of diopside-anorthite melts. *Geophys. Res. Lett.* **18**, 93–96.

Silver L. and Stolper E. M. (1989) Wate in albitic glasses. *J. Petrol.* **30**, 667–709.

Stolper E., Walker D., Hager B. H. and Hays J. F. (1981) Melt segregation from partially molten source regions: the importance of melt density and source region size. *J. Geophys. Res.* **86**(B7), 6261–6271.

Sumita T. and Inoue T. (1996) Melting experiments and thermodynamics analyses on silicate–H2O systems up to 12 GPa. *Phys. Earth Planet. In.* **96**, 187–200.

Suzuki A. and Ohtani E. (2003) Density of peridotite melts at high pressure. *Phys. Chem. Miner.* **30**, 449–456.

Suzuki A., Ohtani E. and Kato T. (1995) Flotation of diamond in mantle melt at high pressure. *Science* **269**, 216–218.

Suzuki A., Ohtani E. and Kato T. (1998) Density and thermal expansion of a peridotite melt at high pressure. *Phys. Earth Planet. In.* **107**, 53–61.

Takahashi E. (1986) Melting of a dry peridotite KLB-1 up to 14 GPa: implications on the origin of peridotitic upper mantle. *J. Geophys. Res.* **91**, 9367–9382.

Toplis M. J. and Richet P. (2000) Equilibrium density and expansivity of silicate melts in the glass transition range. *Contrib. Mineral. Petrol.* **139**, 672–683.

Webb S. and Courtial P. (1996) Compressibility of melts in the $CaO–Al_2O_3–SiO_2$ system. *Geochim. Cosmochim. Acta* **60**(1), 75–86.

Williams Q. and Garnero E. J. (1996) Seismic evidence for partial melt at the base of Earth's mantle. *Science* **273**(5281), 1528–1530.

Zhang J. and Herzberg C. T. (1994) Melting experiments on anhydrous peridotite KLB-1 from 5.0 to 22.5 GPa. *J. Geophys. Res.* **99**, 17,729–17,742.

Zhang J., Li B., Utsumi W. and Liberman R. C. (1996) In situ X-ray observations of coesite–stishovite transition: reversed phase boundary and kinetics. *Phys. Chem. Miner.* **23**, 1–10.

Associate editor: Michael Toplis